A fluid-particle hybrid framework for the PLUTO code: applications to non-thermal emission in jets.

Journal of Physics: Conference Series **719** (2016) 012023 doi:10.1088/1742-6596/719/1/012023

A fluid-particle hybrid framework for the PLUTO code: applications to non-thermal emission in jets.

B. Vaidya[1], A. Mignone[1], G. Bodo[2] and S. Massaglia[1]

[1]Dipartimento di Fisica, University di Torino, via Pietro Giuria 1, I-10125 Torino, Italy
[2]INAF, Osservatorio Astronomico di Torino, Strada Osservatorio 20, I-10025 Pino Torinese, Italy

E-mail: bvaidya@unito.it

Abstract. We present an implementation of a fully parallel hybrid framework for the evolution of Lagrangian particles coupled to a MHD fluid for the PLUTO code. For the applications of interest, particles represent ensembles of electrons whose spectral energy distribution is governed by a kinetic transport equation that takes into account different physical processes such as diffusive shock acceleration, synchrotron emission and adiabatic expansion. An application to model non-thermal emission from extragalactic jets shows the effectiveness and strength of the approach in describing not only the dynamics but also the radiation properties of jets and, in general, of high-energy astrophysical plasma environments.

1. Introduction

Many astrophysical and space physics applications require increasingly complex physics to be included for a more realistic modeling. Depending on the scale of interest, the numerical modeling can be tackled by means of different techniques such as Particle-in-Cell (PIC), multi-fluid or single-fluid MHD.

Recently, hybrid implementations combining both particles and grid-based fluid descriptions have been proposed in order to reduce the large scale gap between macro- and micro-physics. The MHD-PIC approach of [1], for example, describes the interaction between collisionless cosmic ray particles and a thermal plasma. Similarly, [2] proposed a hybrid approach for the BATS-R-US code that combines Hall-MHD and PIC methods in order to capture small-scale kinetic effects in magnetosphere simulations. Other hybrid formulations have been considered to model, e.g., dust (in the Athena code, [3]), collisionless components (in the Enzo code, [4]), Lagrangian test particles (in the Flash code, [5]).

Here we focus on a hybrid particle/fluid approach suitable for treating non-thermal radiation processes from astrophysical plasmas. Previous attempts to include optically thin radiation processes have been proposed by [6] who used passive scalars (fluid tracers) to model synchrotron emission from pulsar wind nebulae and by [7] in the context of jets from radio-galaxies. This approach, however, may become extremely consuming in terms of memory usage as more accurate spectral modeling is needed. A more convenient approach using particles has been proposed by [8] in the context of relativistic jet modeling. Here particles are evolved taking into account radiative losses and their spectral energy distribution allows non-thermal electrons to be injected at shocks. A similar approach was used by [9].

Here we present a fully time-dependent numerical implementation to treat Lagrangian particles describing a population of non-thermal electrons (or protons) dynamically coupled to a MHD fluid. The implementation is fully parallel and part of a more general particle module being developed for the PLUTO code [10] and that will be described in a forthcoming paper. Here we only focus on the static grid implementation. Our formulation is applied to investigate non-thermal emission in extragalactic jets at kilo parsec (kpc) scales where several radio and X-rays observations show the typical imprint of synchrotron emission from highly energetic electrons [11].

2. A Particle Module for the PLUTO Code

A Lagrangian macro-particle (MP) represents an ensemble of real particles (e.g., electrons) sufficiently close in physical space and associated with a sub-grid physical modeling. The position of each MP is determined by the simple transport equation,

$$\frac{d\boldsymbol{x}_p}{dt} = \boldsymbol{v}_p = \boldsymbol{v}\,, \tag{1}$$

where $\boldsymbol{v}$ is the gas velocity.

Each MP is characterized by a distribution function $N(\epsilon, t)$ representing the actual particle number density as a function of energy ϵ. For convenience, energies are distributed in equally-space (in log) bins ranging from $\epsilon_{\rm min}$ to $\epsilon_{\rm min}$ with total of $\mathcal{M}$ bins. The energy distribution changes in time according to several different physical processes, as described in the seminal paper by Kardashev [12]. Here we take into account, for simplicity, only adiabatic compression/expansion and synchrotron radiative losses so that our evolutionary equation becomes

$$\frac{\partial N(\epsilon,t)}{\partial t} = \frac{\partial}{\partial \epsilon}\Big[\left(\alpha(t)\epsilon + \beta(t)\epsilon^2\right) N\Big]\,, \tag{2}$$

where $\alpha(t) = \frac{1}{3}\nabla\cdot\boldsymbol{v}$ represents losses due to adiabatic effects and $\beta(t) \propto \boldsymbol{B}^2$ describes synchrotron losses. Magnetic field and velocity are interpolated from the fluid directly on the particle position. Equation (2) is solved by means of analytical methods by extending the approach of [12] to a general initial energy distribution (not only a power law). The solution is discretized on a *Lagrangian* energy grid and the update is given by the following step :

$$N^{n+1}(\epsilon^{n+1}) = N^n(\epsilon^n) e^a (1 + c\epsilon^n)^2\,, \tag{3}$$

where N^n and N^{n+1} are, respectively, the particle densities at time levels t^n and t^{n+1} in the energy bins ϵ^n and ϵ^{n+1}. In a *Lagrangian* description the bin widths change in time according to

$$\epsilon^{n+1} = \frac{\epsilon^n e^{-a}}{1 + c\epsilon^n}\,, \tag{4}$$

where, to second-order accuracy, a and c are given by

$$\begin{aligned} a &= \int_{t^n}^{t^{n+1}} \alpha(t)dt \approx \tfrac{1}{2}(\alpha(t^{n+1}) + \alpha(t^n))\Delta t. \\ c &= \int_{t^n}^{t^{n+1}} \beta(t)e^{-a}dt \approx \tfrac{1}{2}(\beta(t^{n+1})e^{-a} + \beta(t^n))\Delta t. \end{aligned} \tag{5}$$

If the initial distribution is defined over an interval $[\epsilon_{\rm min},\ \epsilon_{\rm max}]$, this approach does not require specifying explicit boundary conditions and automatically preserves the total number of particles, since

$$\int_{\epsilon^{n+1}_{\rm min}}^{\epsilon^{n+1}_{\rm max}} N^{n+1}(\epsilon) d\epsilon^{n+1} = \int_{\epsilon^{n}_{\rm min}}^{\epsilon^{n}_{\rm max}} N^{n}(\epsilon) d\epsilon^{n}. \tag{6}$$

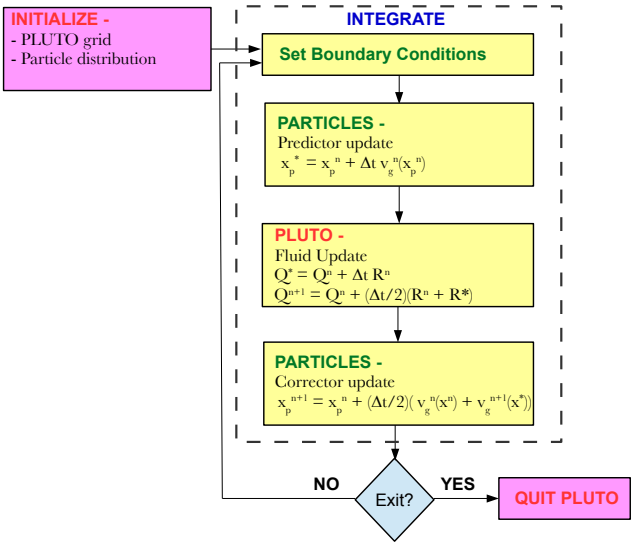

Figure 1. Flowchart for the hybrid Lagrangian particles/fluid update in the PLUTO code.

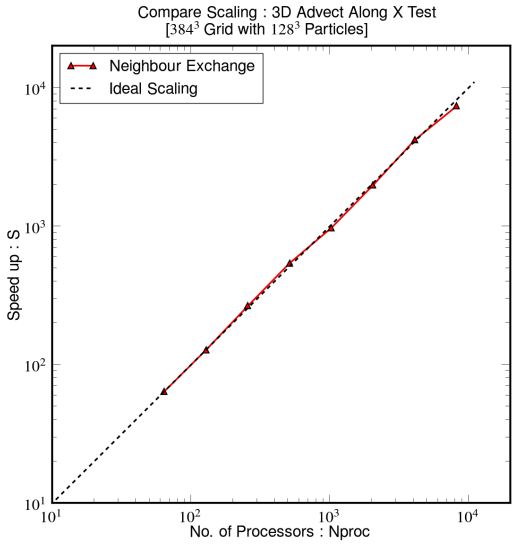

Figure 2. Parallel speedup (strong scaling) for 3D uniform advection problem. The *black dashed* line represents ideal scaling.

In presence of shock waves, the distribution function can change by taking into account diffusive shock acceleration (Fermi I process). However, since the details of the micro-physics are at the unresolved Larmor scale, we employ a sub-grid prescription, under an assumption of isotropy and that the acceleration time scale, $\tau_{\rm acc}$ is much less than dynamical time scale [9]:

$$N_+(\epsilon, t) = \frac{q}{r}\epsilon^{-q+2}\int_{\epsilon_{\rm min}}^{\epsilon} N_-(e,t)e^{q-3}de \tag{7}$$

with $q = 3r/(r-1)$ and the post shock spectrum, N_+, depends on the up-stream particle spectrum N_- and the compression ratio, $r = \rho_+/\rho_-$. Such an assumption is indeed valid for lower energy particles whose emitted radiation is in radio and optical bands. The spectrum update formulation depends on the strength of the shock which is governed by its compression ratio and its direction with respect to magnetic field.

3. Numerical Implementation

The system of fluid+macro-particles (MPs) is governed by the MHD equations (for the fluid) and Eq. (1) for the particle motion. MPs are initialized on the computational domain by prescribing their coordinates and the distribution function $N(\epsilon)$. The same time-marching scheme used for the fluid is also employed to update the particle position; for a $2^{\rm nd}$-order Runge-Kutta scheme, for example, a single time advance is comprised of the steps shown in Fig. 1. Notice that in both the predictor and corrector steps magnetic field and velocity must be interpolated from the fluid grid to the particle position.

The hybrid module has been successfully parallelized using the Message Parsing Interface (MPI) library. We follow a simple approach where each processor updates only the particles lying on its computational sub-domain. Particles must be transferred between neighbors when they cross a processor boundary: in such a way, each processor communicates only with its neighbors. The efficiency of this approach has been tested by timing a simple test consisting of a 3D uniform advection with 384^3 grid cells and 128^3 uniformly distributed MPs. Strong scaling is reported in Fig. 2 for 64 up to 8192 processor showing excellent efficiency (more than 93%).

4. Numerical Benchmarks

In this section, we test our implementation against simple validation benchmarks.

4.1. Stationary Vortex in 2D

The first test case is used to demonstrate the accuracy of our method in tracing the particle evolution along the velocity streamlines. For this purpose, we consider a 2D hydrodynamical stationary vortex configuration [13] for which an analytical solution is available. MPs are initialized in 8 concentric circles at different radii such that 64 particles cover each circumference uniformly. We then track the radial distance for each particle as it evolves and compute the error as a function of time. In Fig. 3 we show the error of a MP initially placed at $r = 2.5$ as a function of time t. They main source of error comes from poorly sampled fluid grid and hence we observe that the maximum error decreases with increasing grid size. At the resolution of 128^2 the errors in radial positions of particles fall below 10^{-7} (red line).

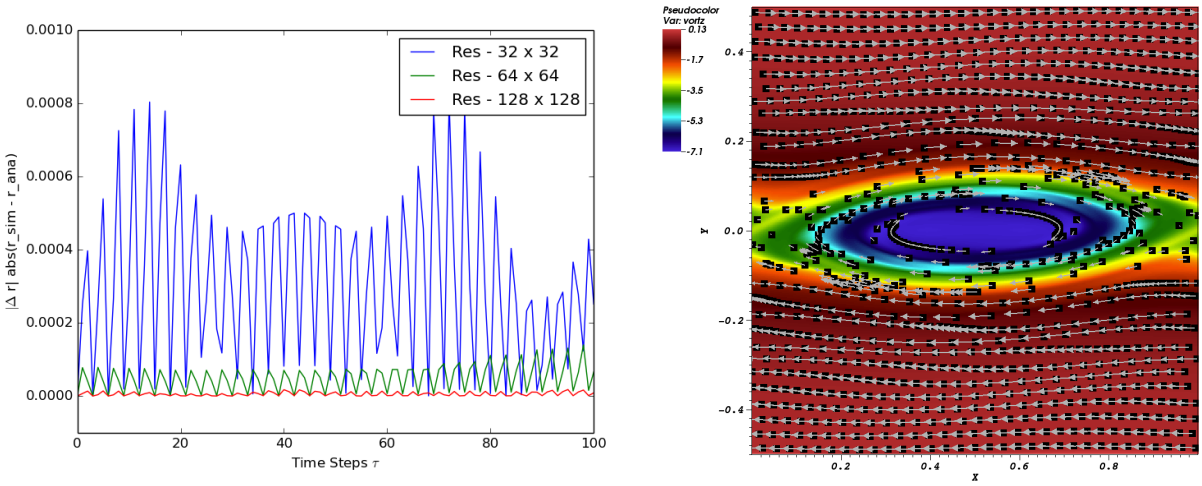

Figure 3. *Left*: error in the radial position for a single particle in the stationary vortex problem at different resolutions. *Right*: evolution of Lagrangian particles in the KH vortex problem. The colormap shows the vorticity while particles and their corresponding velocity are over-plotted.

4.2. Kelvin-Helmholtz Unstable Flow

In the next test we consider a dynamical configuration by simulating the evolution of a 2D shear layer unstable to Kelvin-Helmholtz (KH) instability using the HD module of the PLUTO code. The computational domain is the unit square covered by 512^2 zones with uniform density and pressure. A velocity shear $v_x = V_0 \tanh(y/l)$ with $V_0 = 0.5$ and $l = 0.0637$ is perturbed with a sinusoidal disturbance in v_y with amplitude of 0.01 and a total of 1024 MPs are initially placed uniformly. Periodic boundary conditions are applied in the x direction, while open boundaries are set along y direction. Fig. 3 shows the vorticity of the fluid at $t = 20$ where MPs are represented as black squares and the marked grey arrows (whose lengths are scaled by magnitude of particles velocity) point clearly in the direction of flow as expected.

4.3. Adiabatic Expansion in Sedov-Taylor Blast Wave.

A 2D Sedov-Taylor explosion is set on the unit square using 1024^2 cells and open boundary conditions. We adopt constant density ($\rho = 1$) throughout the domain while the internal energy

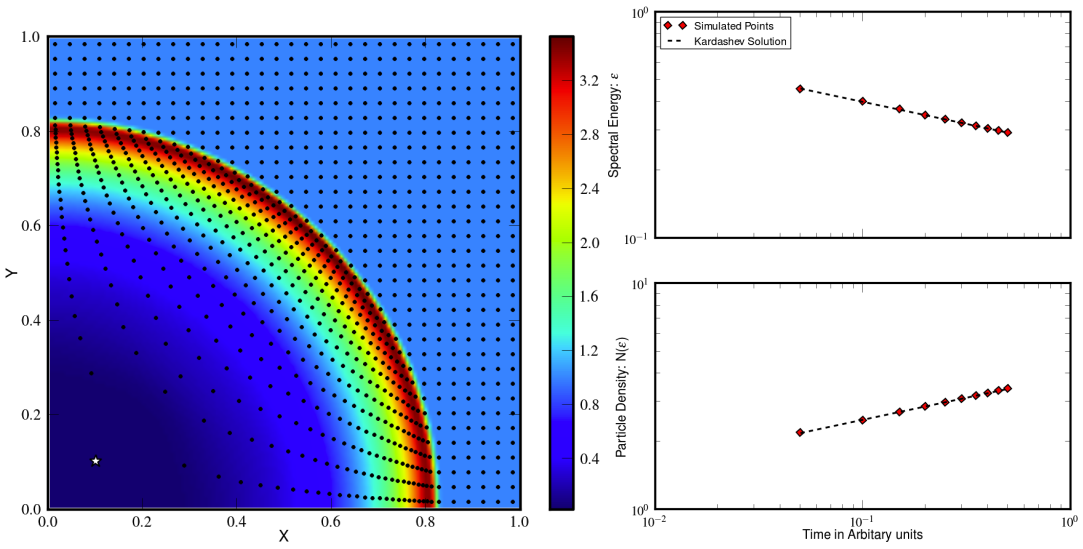

Figure 4. *Left Panel:* Density colormap overlaid with particle distribution (black dots) for the Sedov-Taylor problem at $t = 0.5$. The particle marked as a *white* star is used for further spectral analysis. *Right Panel:* spectral energy evolution for the marked particle in presence of adiabatic expansion only. The *red* squares represent simulation data and black dashed line is the analytical solution [12].

is set to $\rho e = 1.5 \times 10^{-5}$ everywhere except for a small region at the origin where $\rho e = 6.82 \times 10^{3}$. An ideal EoS with adiabatic index $\gamma = 5/3$ is used.

We place a total of 1024 MPs uniformly distributed within the domain and assign to each MP an initial power-law spectrum $N(\epsilon) = N_0 \epsilon^{-\gamma}$ with $\gamma = 3$ covering a range of 6 orders of magnitude in the energy distribution with $\mathcal{M} = 100$ equally-spaced logarithmic energy bins. We solve the hydrodynamical equations (no magnetic field) and, in order to quantify the effect of adiabatic effects only, we do not include shock-acceleration when solving Eq. (2) for the evolution of the distribution function. The solution at $t = 0.5$ is shown in the left panel of Fig. 4. Note that for a very strong shock, the post-shock velocity can be approximated as $v(r, t) \propto r v_s$ where $v_s \propto r_s/t$ and $r_s \propto t^{2/5}$ are the shock front velocity and position, respectively. From this argument, we see that the adiabatic expansion coefficient in Eq. (2) becomes $\alpha \propto 1/t$. Because of this, adiabatic effects modify all energy bins in the same way and the resulting spectral distribution involves a parallel shift of the spectrum, $N(\epsilon)$ without affecting the power-law index γ. This is shown in the right panel of Fig. 4 for a single MP. The analytical dependence of the electrons energy ϵ and of the distribution function $N(\epsilon)$ as a function of time (with $\beta = 0$, no magnetic fields) is presented in [12]. These solutions are over-plotted as *black dashed* lines in middle and bottom panels of Fig. 4. The *red* squares that depicts the value of one of the energy bins for the same particle behind the shock are consistent with the analytical estimates.

4.4. Magnetized Sedov-Taylor Blast Wave.

Next, we consider the effects of synchrotron losses on the evolution of the distribution function in a magnetized cylindrical blast wave simulation. The domain is initially filled with constant density and pressure, $\rho = 1$ and $p = 0.1$ while a constant magnetic field $(B_x, B_y) = (1, 1)$ is prescribed. An over-pressurized region is set inside the circle $r \leq r_0$ (with $r_0 = 0.1$) where $p = 10$. We solve the MHD equations on the 2D Cartesian square $x, y \in [-1, 1]$ using 512^2 zones and place 4096 MPs uniformly with the same spectral distribution used for the previous test.

For the sake of validation, we evolve the MP distribution function by solving Eq. (2) again by neglecting shock acceleration.

The left panel of Fig. 5 shows the particle distribution (black dots) along with the fluid density (colored map) at $t = 0.45$. Owing to the presence of magnetic field, the explosion is no longer symmetric but proceeds faster along magnetic field lines. The particle number density decreases at the center where a strong rarefaction takes place and is enhanced behind the oval-shaped slow shock along the main diagonal. In the same figure, two MPs of interest from the point of view of spectral evolution are marked as *green* and *red* diamonds. The spectral evolution for the *green* particle is shown in top right panel of Fig. 5 where we plot $\epsilon^2 N(\epsilon)$ as a function of the energy ϵ. The initial power-law distribution shows a systematic shift towards lower energies right after $t \approx 1$. This takes place as the shock wave traverses through this particle resulting in an expanding flow around it. The subsequent evolution of the distribution function is mainly determined by synchrotron emission losses which produces a steeper spectrum at higher energies.

The evolution of the highest energy bin for both marked MPs is shown in the left panel of Fig. 6 where the *black dashed* line is Kardashev's solution of Eq. (2) with $\alpha = 0$, implying losses only due to synchrotron emission. As expected, the highest spectral energy bin of the unshocked *red* MP is consistent with the analytical estimate as it is unaffected by any adiabatic effect. On the contrary, the distribution function of the *green* evolve under the combined effects of adiabatic expansion and synchrotron losses. For both of the marked MPs, the normalized particle density in the highest energy bin, $(N(\epsilon_{\rm max})/N_0)\epsilon^\gamma$ decays with time. The green particle decays at a higher rate as it suffers both synchrotron and adiabatic losses (see right panel of Fig. 6). This test clearly demonstrates the different effects of the two radiative loss terms that are considered in the present work.

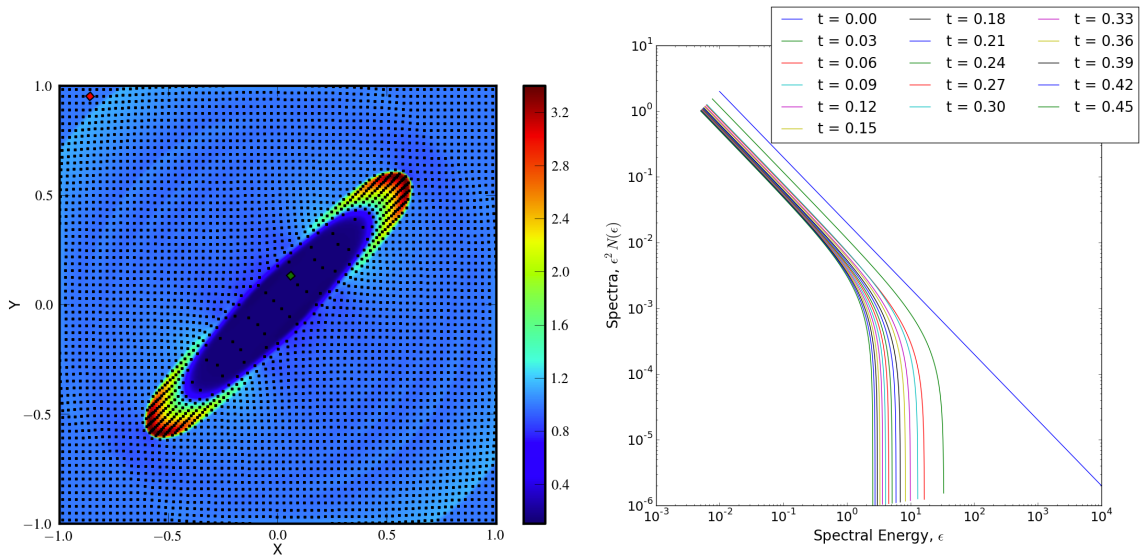

Figure 5. *Left Panel:* Density (colormap) and particle distribution (black dots) in the oblique MHD shock problem. Particles marked in *green* and *red* are used for further analysis. *Right Panel:* spectral evolution of the green-marked particle at different times.

4.5. Application to AGN Jets

A large body of observational evidence indicates that jets from active galactic nuclei (AGN) in FRI sources undergo significant deceleration at the kpc scale and slow down to mildly relativistic

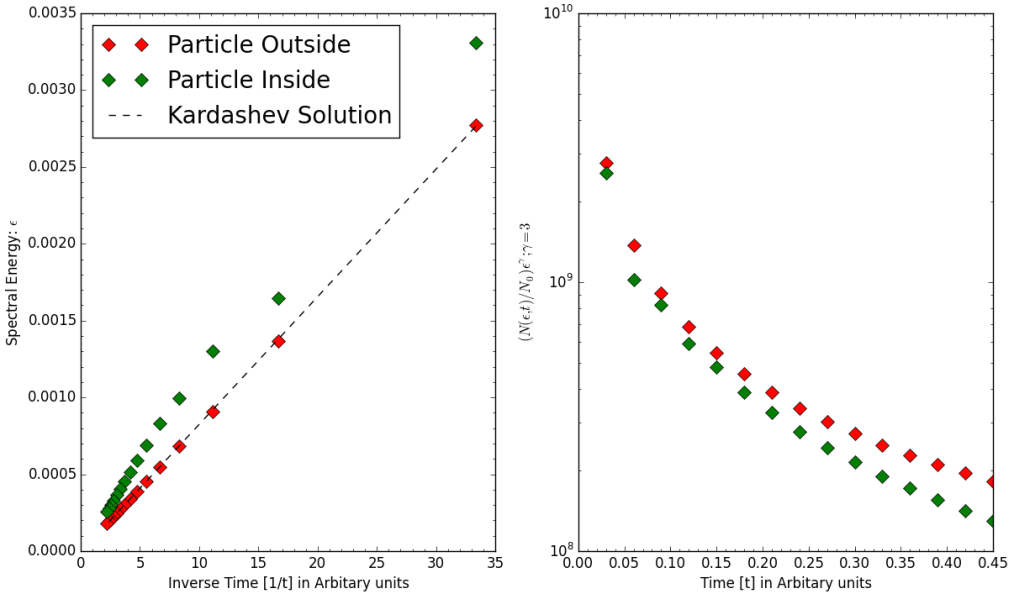

Figure 6. *Left panel:* time evolution of the largest energy bin for the marked particles (red and green squares) compared to the analytical expectation. *Right Panel:* time evolution of the normalized particle density for the largest energy bin, $(N(\epsilon)/N_0)\epsilon^{\gamma}$, with $\gamma = 3$ for the two marked particles.

speeds with a typical bulk Lorentz factor $\Gamma \sim 2$ [14]. We employ our particle module to investigate the physical processes responsible for the non-thermal emission of AGN jets observed at these scales.

To this purpose we now focus on the evolution of a magnetized jet in 2D cylindrical coordinates (r, z) and consider a computational domain with size of $r_{\rm max} = 3.2$ kpc and $z_{\rm max} = 12.8$ kpc and has a resolution of ~ 12.5 pc. The ambient medium is non-magnetized and stratified in density, $\rho = 1/(1 + R^2)$ where $R = \sqrt{r^2 + z^2}$ is the spherical radius. We prescribe constant pressure $p_0 = 1/\gamma$ so that the sound speed is unity at the origin. A pressure-matched supersonic beam with lower density ($\rho_j = 10^{-2}$) is injected through a nozzle of radius $r_j = 100$ pc at $z = z_{\rm min}$ with velocity $v_j = 4$. The jet carries a purely toroidal magnetic field $B_\phi = 100\mu G$, compatible with observational estimates. Macro-particles are initially placed inside the domain but also as injected at regular time intervals through the nozzle with an initial power-law distribution function of the form $N(\epsilon) \propto \epsilon^{-3}$. Energy bins cover a range of 6 orders of magnitude in energy from 10^{-4} to 100 ergs. so that the resulting emission spans from radio to X-ray wavelength. We follow their evolution through Eq. (1)-(2) and model shock acceleration through Eq. (7).

The left panel of Fig. 7 shows the jet tracer and the corresponding MPs distribution at $t \sim 0.5\, Myr$. At this time, a total number of $\gtrsim 1.3 \times 10^5$ MPs cover the whole jet. In the right panel of Fig. 7 we show the spectral evolution and the trajectory of a representative MP that is introduced through the jet nozzle at time $t \approx 26.3$. The initial power law spectrum (black line) undergoes strong synchrotron losses resulting in a steeper spectrum (red curve) at $t \approx 27$. After this time, the distribution function flattens (green curve with power-law index $\gamma \approx -2.3$) as the particle crosses an internal shock surface. Subsequently, the MP is pushed out the shocked region and encounters a turbulent magnetized region where its spectrum becomes steeper and the distribution function progressively moves to the radio wavelengths. Similar effects are seen in several other MPs, although particles that never enter the shock also continuously loose energy

over time.

In order to investigate the collective effect of all particles on the emitted radiation we estimate the emissivity $J(\nu)$ by consistently employing the spectra of each MP at various instants during the simulation. The emissivity is related to the spectral distribution as follows:

$$J(\nu) = \int_0^\infty j(x)N(\epsilon)d\epsilon = 4\pi \frac{dI(\nu)}{dl}\,, \tag{8}$$

where $j(x)$ is the emissivity of a single electron, $x = \nu/\nu_c$ and $\nu_c = 3\pi\gamma_e^3\nu_0$ is the critical frequency function of the electron energy and orbital frequency ν_0. For an optically thin medium, the emissivity can be related to the observed intensity $I(\nu)$ as shown above with l being the length along line of sight. In Fig. 8 we show the distribution of $J(\nu)$ at two different frequencies, $\nu = 1.6$ GHz and $\nu = 15$ GHz typically used to observe AGN jets with radio interferometers such as VLA and VLBI. The left and middle panels show the distribution at 1.6 GHz without (left) and with (middle) shock acceleration, Eq. (7). Brighter emission in proximity of the bow shock and at the internal knots is observed when Fermi-I process is considered via sub-modelling. In addition, we see a large fraction of diffused faint emission from older population of MPs in the turbulent regions of the jet. This effect is more pronounced in the middle panel as particles tend to be re-accelerated at small scale shocks. The distribution of $J(\nu)$ for 15 GHz is evidently different from the one obtained at 1.6 GHz. The high energy radio band only tracks particles at the shock that are able to resist the cooling due to synchrotron emission.

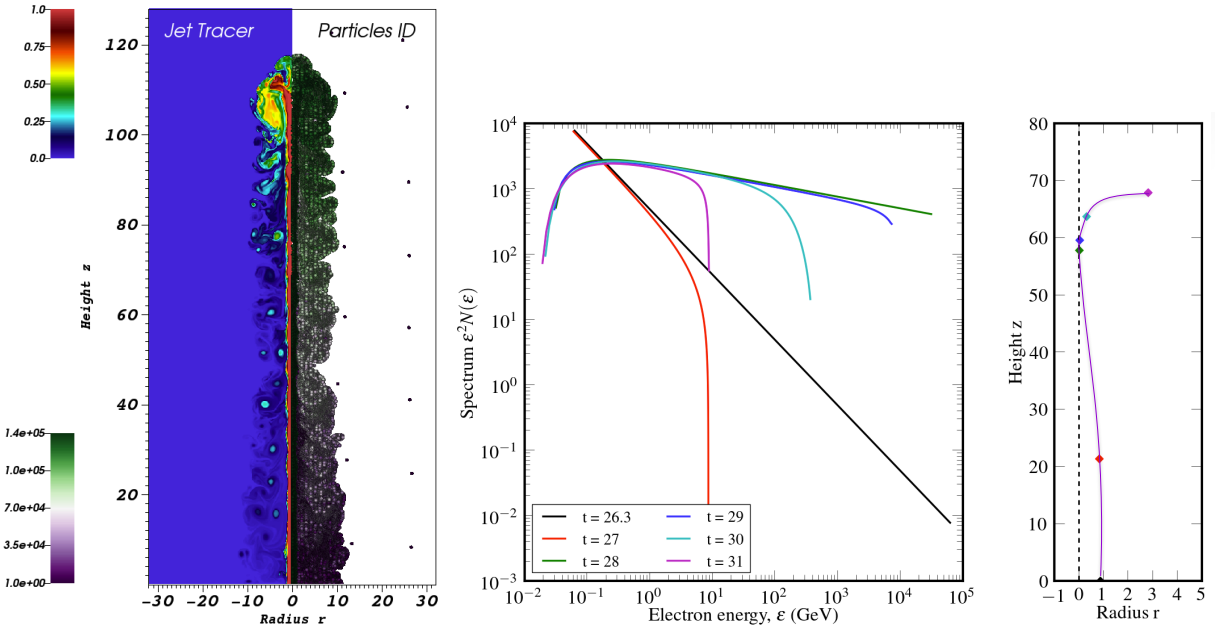

Figure 7. *Left Panel:* Jet tracer (*left half*) and particles ID (*right half*) for the reference run described in Sec. 4.5. Particles are labeled by increasing injection ID. Green particles have been injected more recently and are responsible for the bulk of emission. Purple particles have been introduced at earlier stages of the evolution and have already cooled down. *Middle panel:* spectral evolution of a representative particle. *Bottom panel:* particle trajectory. The same color key used in the middle panel is applied.

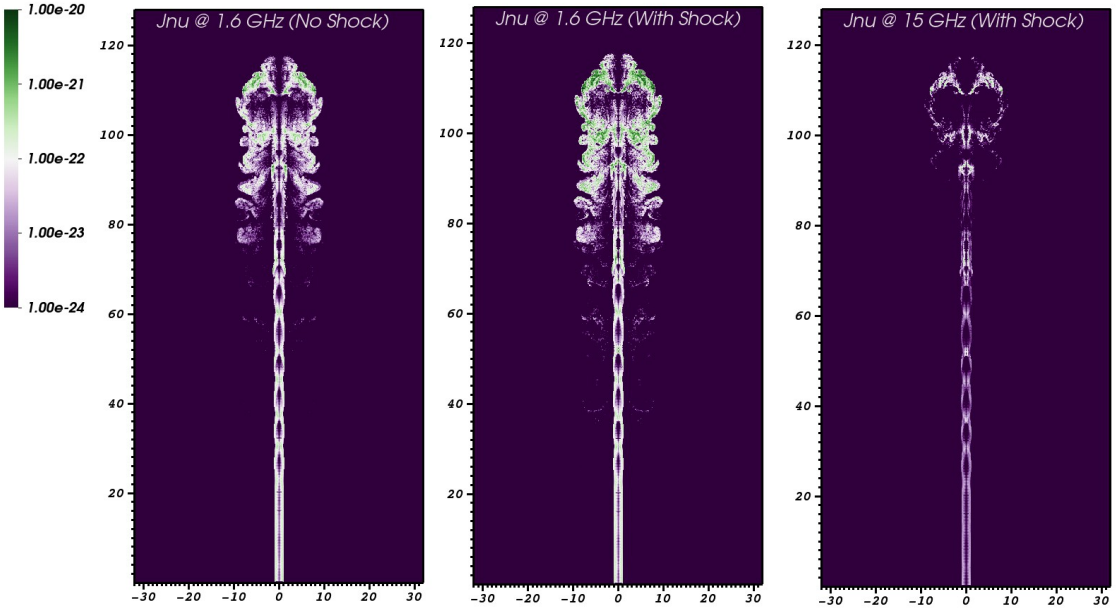

Figure 8. Emissivity, $J(\nu)$ [in ergs $s^{-1}Hz^{-1}cm^{-1}$], at 1.6 GHz (*left* and *middle* panels) and 15 GHz (*right* panel). The effects due to shock acceleration are switched off in the *left* panel.

5. Discussion & Summary

We have developed a fully parallel, hybrid module incorporating *Lagrangian* particles in the static grid version of the PLUTO code. A single macro-particle can be thought as a swarm of real particles (e.g. electrons) whose spectral energy distribution can be described using a convection-diffusion transport equation. For the present purpose, only adiabatic effect, synchrotron losses and shock-acceleration have been included. The numerical algorithm for fluid/particle evolution together with the parallelization strategy have been presented. Numerical benchmarks demonstrating the correctness of the implementation have been illustrated by a direct comparison with analytical solutions. The adaptive mesh implementations will be addressed in an upcoming work.

Furthermore, we have presented axisymmetric MHD simulations of jets aimed at studying the competition between the shock acceleration mechanism and various radiation losses in the context of kpc-scale extragalactic jets. We find that internal knots formed in the jet become efficient sites for particle acceleration capable of producing flat spectra with power-law indices that are consistent with the theory of diffusive shock acceleration. However, we also see that for typical magnetic fields inferred from observations, the losses eventually dominates producing a steeper spectrum at radio wavelengths. This suggests that additional mechanisms must operate to continuously re-accelerate particles in order to sustain the emission over longer time spans. In this sense, magnetic reconnection and turbulent scattering (Fermi II order) acting in the jet cocoon are among the most promising candidates. These possibilities will be explored in forthcoming papers along with 3D relativistic jet simulations.

References

[1] Bai X N, Caprioli D, Sironi L and Spitkovsky A 2015 *The Astrophysical Journal* **809** 55 (*Preprint* `1412.1087`)
[2] Daldorff L K S, Tóth G, Gombosi T I, Lapenta G, Amaya J, Markidis S and Brackbill J U 2014 *Journal of Computational Physics* **268** 236–254
[3] Bai X N and Stone J M 2010 *Astrophysical Journal Suppl.* **190** 297–310 (*Preprint* `1005.4980`)

[4] Bryan G L, Norman M L, O'Shea B W, Abel T, Wise J H, Turk M J, Reynolds D R, Collins D C, Wang P, Skillman S W, Smith B, Harkness R P, Bordner J, Kim J h, Kuhlen M, Xu H, Goldbaum N, Hummels C, Kritsuk A G, Tasker E, Skory S, Simpson C M, Hahn O, Oishi J S, So G C, Zhao F, Cen R, Li Y and Enzo Collaboration 2014 *Astrophysical Journal Suppl.* **211** 19 (*Preprint* `1307.2265`)
[5] Dubey A, Daley C, ZuHone J, Ricker P M, Weide K and Graziani C 2012 *Astrophysical Journal Suppl.* **201** 27
[6] Del Zanna L, Volpi D, Amato E and Bucciantini N 2006 *A&A* **453** 621–633 (*Preprint* `astro-ph/0603080`)
[7] Tregillis I L, Jones T W and Ryu D 2001 *The Astrophysical Journal* **557** 475–491 (*Preprint* `astro-ph/0104305`)
[8] Mimica P, Aloy M A, Agudo I, Martí J M, Gómez J L and Miralles J A 2009 *The Astrophysical Journal* **696** 1142–1163 (*Preprint* `0811.1143`)
[9] Micono M, Zurlo N, Massaglia S, Ferrari A and Melrose D B 1999 *A&A* **349** 323–333 (*Preprint* `astro-ph/9906440`)
[10] Mignone A, Bodo G, Massaglia S, Matsakos T, Tesileanu O, Zanni C and Ferrari A 2007 *Astrophysical Journal Suppl.* **170** 228–242 (*Preprint* `astro-ph/0701854`)
[11] Hardcastle M 2015 Kiloparsec-Scale AGN Jets *The Formation and Disruption of Black Hole Jets* (*Astrophysics and Space Science Library* vol 414) ed Contopoulos I, Gabuzda D and Kylafis N p 83
[12] Kardashev N S 1962 *Soviet Astronomy* **6** 317
[13] Chi-Wang S 2001 High order finite difference and finite volume weno schemes and discontinuous galerkin methods for cfd Tech. rep.
[14] Laing R A and Bridle A H 2013 *Monthly Notices in Royal Astronomy* **432** 1114–1132 (*Preprint* `1303.6664`)